Radiative heating characteristics of Earth's cloudy atmosphere from vertically resolved active sensors

John M. Haynes,[1] Thomas H. Vonder Haar,[1,2] Tristan L'Ecuyer,[3] and David Henderson[2]

Received 7 November 2012; revised 27 December 2012; accepted 5 January 2013; published 13 February 2013.

[1] High vertical resolution CloudSat radar measurements, supplemented with cloud boundaries and aerosol information from the CALIPSO lidar, are used to examine radiative heating features in the atmosphere that have not previously been characterized by passive sensors. The monthly and annual mean radiative heating/cooling structure for a 4 year period between 2006 and 2010 is derived. The mean atmospheric radiative cooling rate from CloudSat/CALIPSO is $0.98\,\mathrm{K\,d^{-1}}$ ($1.34\,\mathrm{K\,d^{-1}}$ between 150 and 950 hPa) and is largely a reflection of the Earth's mean water vapor distribution, with sharp vertical gradients introduced by clouds. It is found that there is a minimum in cooling in the tropical lower to middle troposphere, a cooling maximum in the upper-boundary layer of the Southern Hemisphere poleward of $-10°$ latitude, and a minimum in cooling in the lower boundary layer in the middle to high latitudes of both hemispheres. Clouds tops tend to strongly cool the upper-boundary layer all year in the midlatitudes to high latitudes of the Southern Hemisphere (where peak seasonal mean winter cooling is $3.4\,\mathrm{K\,d^{-1}}$), but this cooling is largely absent in the corresponding parts of the Northern Hemisphere during boreal winter, resulting in a hemispheric asymmetry in cloud radiative cooling. **Citation:** Haynes, J. M., T. H. Vonder Haar, T. L'Ecuyer, and D. Henderson (2013), Radiative heating characteristics of Earth's cloudy atmosphere from vertically resolved active sensors, *Geophys. Res. Lett.*, *40*, 624–630, doi:10.1002/grl.50145.

1. Introduction

[2] The heating of the atmosphere by radiative processes is an important component of the energy budget of the Earth system. In the annual mean, the atmosphere loses approximately $112\,\mathrm{W\,m^{-2}}$ through shortwave and longwave radiative processes, and this loss is nearly compensated by latent and sensible heat fluxes from the surface [*Stephens et al.*, 2012]. Clouds play an important role in this radiative imbalance, and these cloud effects feed back into the atmosphere's general circulation in a number of profound ways [e.g., *Slingo and Slingo*, 1988, 1991].

[3] Some of the earliest measurements of infrared radiative heating in the atmosphere were via flux measurements from balloon-borne plate radiometers [e.g., *Kuhn and Suomi*, 1960; *Suomi and Kuhn*, 1958]. Additional estimates were provided by *Davis* [1963] and the radiative-convective equilibrium study of *Manabe and Strickler* [1964]. Since it was very early in the satellite era, both studies utilized crude estimates of Earth's mean cloudiness and considered gross height distributions of overcast cloud layers. Still, their estimated mean lower-tropospheric cooling rate of between 1 and $2\,\mathrm{K\,d^{-1}}$ is remarkably consistent with modern estimates.

[4] The beginning of the satellite era in the 1960s brought the first estimates of radiative heating from satellite [*Sabatini and Suomi*, 1962], and over the coming decades satellites greatly improved our knowledge of the Earth's radiation budget and the horizontal distribution and radiative effects of clouds [*Hartmann and Short*, 1980; *Vonder Haar and Suomi*, 1971]. Until the 21st century, nearly all satellite-based observations of cloud-sized hydrometeors were passive, meaning they were obtained by measuring the sunlight reflected by the Earth system and thermal emission by the same. Although these measurements are well suited to characterize the horizontal distribution of clouds, they are not ideal for resolving vertical cloud structure, and as a result information about the radiative heating of the atmosphere as derived from vertically constrained cloud observations was largely limited to data from fixed ground-based cloud radars [e.g., *McFarlane et al.*, 2007] and field campaigns [e.g., *Johnson and Young*, 1983].

[5] To circumvent these limitations, the present-day International Satellite Cloud Climatology Project (ISCCP) utilizes retrievals of cloud optical depth and cloud top temperature from geostationary and polar orbiting satellites, along with a statistical cloud vertical structure database, to drive a radiative transfer model that produces radiative fluxes at the surface, top of atmosphere (TOA), and three vertical levels within the atmosphere (the ISCCP-FD data set) [*Rossow and Zhang*, 1995; *Zhang et al.*, 1995, 2004]. Similarly, the Surface and Atmospheric Radiative Budget working group uses TOA fluxes observed by the CERES instrument [*Wielicki et al.*, 1996] to constrain a radiative transfer model and produce fluxes at the same number of vertical levels as ISCCP [*Kato et al.*, 2005]. These techniques produced the first global-scale estimates of radiative heating within the atmosphere and at the surface, but multilayered clouds and ambiguity in cloud base remained problematic, so the vertical profile of global radiative heating remained poorly resolved.

[1]Cooperative Institute for Research in the Atmosphere, Colorado State University, Fort Collins, CO, USA.
[2]Department of Atmospheric Science, Colorado State University, Fort Collins, CO, USA.
[3]Department of Atmospheric and Oceanic Sciences, University of Wisconsin-Madison, Madison, WI, USA.

Corresponding author: John M. Haynes, Cooperative Institute for Research in the Atmosphere, Colorado State University, Fort Collins, CO, 80523. (john.haynes@colostate.edu)

0094-8276/13/10.1002/grl.50145

[6] This changed with the 2006 launch of the Cloud Profiling Radar (CPR) onboard CloudSat [*Stephens et al*., 2002, 2008] and the CALIOP lidar (Cloud-Aerosol Lidar with Orthogonal Polarization) onboard CALIPSO (Cloud-Aerosol Lidar and Infrared Pathfinder Satellite Observations) [*Winker et al*., 2007]. When combined, data from these two active sensors provide a near-global view of the tops and bases of most radiatively active clouds in the Earth's atmosphere. Results from this new data set indicated that multiple-layer clouds are ubiquitous [*Haynes and Stephens*, 2007; *Mace et al*., 2009], and passive sensors largely fail to resolve their vertical boundaries [*Haynes et al*., 2011; *Mace*, 2010]. To leverage the vertical resolving capabilities of the new active sensors, a radiative flux retrieval (2B-FLXHR) was developed for the CPR that uses the CloudSat microphysical retrievals as inputs to a radiative transfer model [*L'Ecuyer et al*., 2008, hereafter L08]. L08 reported that outgoing longwave (LW) and shortwave (SW) fluxes calculated using this method exhibited good agreement with CERES on timescales of a week or greater and in areas of 5° latitude/longitude or larger, but the largest uncertainties in this retrieval were related to the inability of the CPR to resolve low clouds within the radar's ground clutter region below 1 km. High, thin clouds were also identified as a source of uncertainty.

[7] Both of these limitations have been largely overcome in the new CloudSat 2B-FLXHR-LIDAR product which supplements the CloudSat cloud boundaries with CALIPSO cloud observations and also utilizes lidar-based aerosol retrievals [*Henderson et al*., 2012]. We use this new product to analyze radiative heating rates in the atmosphere, paying particular attention to the vertical gradients that are not well resolved by passive remote sensing methods. Section 2 contains the data sets and methodology used in this study. Section 3 contains the results and section 4 a discussion and conclusions.

2. Data and Methods

[8] The high-resolution vertical cloud information used in this study comes from two active sensors that are part of the A-Train constellation, the CPR radar aboard CloudSat, and the CALIOP lidar aboard CALIPSO. The CPR operates at 94 GHz and is near-nadir pointing, with a vertical resolution of 480 m (oversampled to 240 m) and a footprint of approximately 1.4 km cross-track and 1.7 km along-track [*Stephens et al*., 2008; *Tanelli et al*., 2008]. The radar cloud mask is supplemented by near-simultaneous measurements of cloud boundaries from CALIOP [*Winker et al*., 2007]. Cloud is considered to occur anyplace that either the radar indicates cloud with high confidence (a cloud mask value of 30 or greater), or the lidar indicates 50% or greater cloud content within the radar bin.

[9] Radiative heating rates were calculated from the R04 2B-FLXHR-LIDAR product [*Henderson et al*., 2012; *L'Ecuyer et al*., 2008], which uses the CloudSat microphysical retrievals and combined CloudSat/CALIPSO cloud mask as inputs to a broadband, two-stream, plane-parallel, adding and doubling radiative transfer model. The model produces upward and downward fluxes at 240 m vertical increments.

[10] Since the A-Train orbit has a fixed equatorial crossing time (approximately 0130 and 1330 h local solar time), the fluxes in 2B-FLXHR-LIDAR are biased toward the local time of observation. To partially mitigate this bias, we follow the method used in L08 whereby instantaneous SW flux estimates, F_{CC}, are corrected so that they better represent the average daily flux, F, using

$$F = F_{cc}\left(\frac{\overline{F_{\text{day}}}}{F^{\downarrow}_{\text{TOA}}}\right), \tag{1}$$

where $\overline{F_{\text{day}}}$ is the average TOA insolation for the pixel's latitude and day of year, and $F^{\downarrow}_{\text{TOA}}$ is the instantaneous TOA insolation. After applying this correction to the SW fluxes, flux profiles are converted to heating rates using

$$\frac{dT}{dt} = \frac{g}{c_p}\frac{dF_{\text{net}}}{dp}, \tag{2}$$

where T is temperature, t is time, g is the gravitational constant, c_p is the specific heat capacity of dry air, p is pressure, and F_{net} is the corrected net flux passing through that level. Thermodynamic information used for calculation of clear-sky fluxes is obtained from the CloudSat ECMWF-AUX product. For comparison purposes, CERES heating rates are calculated in the same manner using the Cloud and Radiative Swath (CRS) Level 2, edition 2C data set for Aqua [*Wieliki et al*., 1996].

[11] Uncertainties in column heating rates can be estimated from uncertainties in TOA and surface fluxes [*Henderson et al*., 2012, Table 1]. Neglecting covariance between fluxes and taking the square root of the sum of square uncertainties in upward and downward fluxes at the TOA and surface, we find the uncertainties in column SW, LW, and total heating to be 12.5%, 12.5%, and 17.7%, respectively. Note that uncertainties near cloud boundaries, where vertical flux gradients can be large, may be larger than these column estimates.

3. Results

[12] The annual average all-sky radiative heating derived from CloudSat/CALIPSO for December 2006 through November 2010 (henceforth the 4 year period) and from CERES for 2007 are shown in the top panels of Figure 1 (note that the CERES heating rates, which are available in four vertical layers, have been expanded vertically to match the radar resolution). The bottom panels show the standard deviation of the same. The time periods are mismatched because CERES CRS data are not available after 2007, but we note that CloudSat/CALIPSO results for 2007 are visually similar to those shown for the entire 4 year period. The SW and LW components of heating are calculated at local time of observation, which is nearly identical for both instruments, and the SW fluxes are corrected as described in section 2.

[13] For the time periods shown in Figure 1, the mean atmospheric radiative cooling rate from CloudSat/CALIPSO is $0.98\,\text{K}\,\text{d}^{-1}$ ($1.34\,\text{K}\,\text{d}^{-1}$ between 150 and 950 hPa) and from CERES is $0.93\,\text{K}\,\text{d}^{-1}$ ($1.33\,\text{K}\,\text{d}^{-1}$ between 200 hPa and the surface). Although both instruments show similar tropospheric cooling rates, the distributions in space and time are quite different. Gross structures present in the CloudSat/CALIPSO view of annual mean heating include (1) a minimum in cooling in the tropical lower to middle troposphere, (2) a maximum in cooling at about 775 hPa in the Southern Hemisphere poleward of −10° latitude, and (3) a minimum in cooling at about 925 hPa in the middle to high latitudes. CERES-derived heating rates, by contrast,

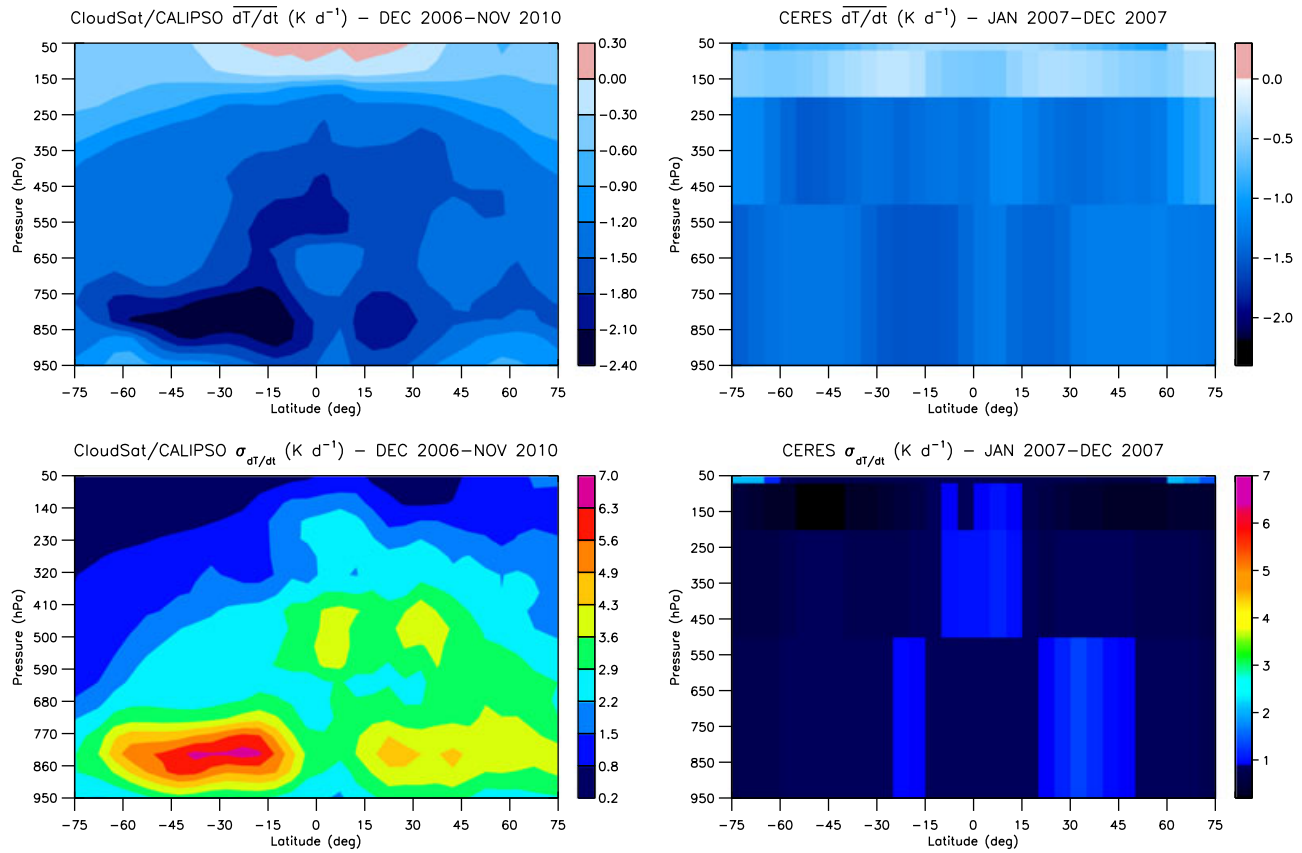

Figure 1. Annual mean net radiative heating rate (top panels) and the standard deviation thereof (bottom panels) as a function of latitude and pressure. CloudSat/CALIPSO-derived values for the 4 year period beginning December 2006 are at left, and CERES-derived values for the year beginning January 2007 (with the four vertical levels expanded vertically to match the radar resolution) are at right.

have less latitudinal structure and smaller corresponding variances. The midlatitude structure is considerably different; in the Southern Hemisphere, for example, the cooling peak for CERES is in the upper troposphere, while CloudSat/CALIPSO places particularly strong cooling in the lower troposphere. This mismatch demonstrates a limitation of the passive technique when cloud obscures a lower cloud layer, as commonly occurs in this region [*Haynes et al.*, 2011; *Mace et al.*, 2009]).

[14] As all of these features are cloud-related, it is first instructive to define the cloud radiative heating (CRH). The CRH at a given atmospheric level is defined as the all-sky minus clear-sky radiative heating rate; it is the radiative heating contribution to the atmosphere at a given level that arises from the presence of clouds anywhere in the same vertical column. Note that, similar to the concept of cloud radiative forcing (sometimes called cloud radiative effect), it does not include feedbacks; it is simply the portion of the radiative heating that would be absent if clouds were instantaneously removed from the scene.

[15] The observed CloudSat/CALIPSO cloud fraction for two seasonal subsets of the 4 year period, December through February (DJF) and June through August (JJA), are shown in Figure 2. Some significant features are the frequent occurrence of cloud in the midlatitudes associated with extratropical cyclones, a lack of clouds in the subtropics associated with the descending branch of the Hadley cell (excluding marine stratus found in the lowest levels), and enhanced cloudiness in the tropics resulting from convection and associated cirrus. The maximum in tropical cloudiness shifts across the equator with the seasonal movement of the intertropical convergence zone, and the amount of upper tropospheric cloudiness between about 15° and 45° latitude is largest in the summer hemisphere. Of particular note is a hemispheric asymmetry in cloud fraction below 600 hPa in the region between 45° and 75° latitude. The Southern Hemisphere (SHEM) is cloudier than the Northern Hemisphere (NHEM), and the decrease in cloudiness during the summer months is less pronounced than in the NHEM. With these patterns of cloudiness in mind, we now discuss the CloudSat/CALIPSO-derived clear-sky radiative heating rates and then how clouds modify this background state.

[16] Clear-sky cooling varies with both location and season (Figure 3, middle column). In the LW, tropospheric clear-sky cooling rates are largest in the tropics, a result of emission by an atmosphere rich in low-level water vapor that is mixed vertically by convective processes. The LW clear-sky cooling is, on average, smaller in the midlatitudes and high latitudes, with the NHEM experiencing more cooling during its summer than the SHEM. Clear-sky SW heating is large in the tropics, chiefly due to absorption by water vapor and oxygen. It is also large in the high latitudes of the summer hemisphere due to the long day length.

[17] The left and right columns of Figure 3 show the all-sky heating rates and resultant CRH, broken into SW and LW components. The SW CRH is, in the annual mean, 2.1 times

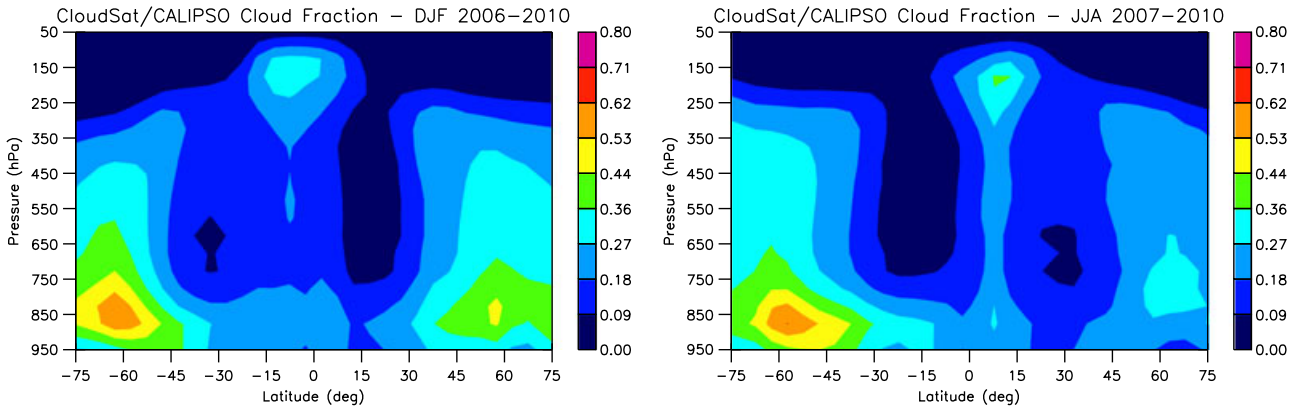

Figure 2. Cloud fraction for DJF 2006–2010 (left) and JJA 2007–2010 (right).

smaller than the LW CRH (note the differing scales). High clouds tend to reduce SW absorption by the underlying atmosphere, while low clouds tend to enhance it by increasing the geometric path length of photons, thus increasing the probability of absorption. The Cloudsat/CALIPSO-derived SW CRH is consistent with both these ideas: it is maximum in the tropical upper troposphere, where cirrus are ubiquitous, and also large in the subtropics and midlatitudes of the summer hemisphere, where low cloud occurs in the presence of a low summertime solar zenith angle. This zone of stronger SW CRH also extends into the lower troposphere, especially in the higher latitudes where low clouds are particularly prevalent.

[18] LW cloud radiative heating is larger than SW and drives the structure of the features highlighted in Figure 1. In fact, the mean atmospheric radiative heating is largely a reflection of the Earth's mean water vapor distribution, punctuated by vertical gradients introduced by clouds. Figure 3 shows a local minimum in total LW cooling (maximum in LW CRH) in the tropical lower and middle troposphere. As demonstrated in L08, this is a result of enhanced infrared cloud radiative warming by high-topped clouds, particularly cirrus that prevent LW radiation from escaping to space, while also radiating toward the surface. The resulting atmospheric heating is maximized in the lower and upper troposphere, but the tropical region near 550 hPa actually experiences cloud-related cooling. The more convectively active portions of the tropics, such as the West Pacific and Indian Ocean basins, have been observed to contain a peak in midlevel clouds, probably associated with a climatological mean stable layer near the height of the freezing level [e.g., *Haynes and Stephens*, 2007; *Johnson et al*., 1999].

[19] The area of strong infrared cooling (and negative LW CRH, i.e., cloud radiative cooling) near 775 hPa is dominated by emission from cloud tops, especially over the SHEM where the maximum mean JJA cooling is 3.4 K d^{-1}. *Haynes et al*. [2011] reported a 3 year, area-averaged cloud fraction from Cloudsat/CALIPSO of 0.81 for the region between 30°S and 65°S and showed that clouds with average tops near 2.5 km (or approximately 750 to 800 hPa) dominate this region. Low clouds are also common in the middle to high latitudes of the NHEM [e.g., *Mace*, 2010], but they cover a smaller fraction of the total area and therefore have a reduced radiative impact. It is not surprising, therefore, that there is a hemispheric asymmetry in radiative cooling at 775 hPa, with the SHEM midlatitudes to high latitudes undergoing radiative cooling during the entire year, while the corresponding latitudes in the NHEM cool during the boreal winter and warm during the boreal summer.

[20] Another feature is an area of reduced cooling in the low levels (enhanced LW CRH) apparent in both hemispheres in the vicinity of 925 hPa. This is a result of infrared warming from cloud bases and is largest when a cold boundary layer overlies a relatively warm surface. During the NHEM summer, the region of enhanced low-level LW CRH persists even where the overlying cloud radiative cooling is largely absent. This occurs because the clear-sky component of the cooling is also large, which we speculate is due to relatively high water vapor concentration in the upper-boundary layer during the NHEM summer.

[21] The month-by-month evolution of these features is shown in the Hovmöller diagrams of Figure 4. Near the tropopause at 175 hPa, latitudes poleward of 30° experience cloud-related cooling all year, while the tropics warm on average. At 575 hPa, the tropics and higher latitudes are cooled by clouds, while the subtropics and midlatitudes are warmed. There is some seasonality in the NHEM between about 45° and 65° in that warming is present during the summer months, while cooling is present during the winter. This likely reflects the relatively large increase in cloud cover during the NHEM winter as compared to the SHEM (see Figure 2). At 775 hPa, seasonality is present in both hemispheres. The peak tropical cloud-related warming follows the mean position of the Intertropical Convergence Zone, and at higher latitudes cloud radiative cooling is maximized during the winter. In the NHEM, however, the sign of CRH changes to produce warming in the midlatitudes, while clouds at this level in the atmosphere always cool, on average, in the SHEM. This again reflects the observation that the SHEM midlatitudes have a high frequency of cloud occurrence during the entire year, while the NHEM experiences a decrease in clouds during the boreal summer.

4. Discussion and Conclusions

[22] This work quantifies the bulk features of atmospheric radiative heating for a multiyear period as derived from CloudSat radar and CALIPSO lidar measurements, using radiative fluxes from the new CloudSat 2B-FLXHR-LIDAR product. The longwave CRH is about twice as large as the shortwave CRH in this analysis, a result of the fact that most clouds scatter far more shortwave radiation than they absorb. Therefore, the mean atmospheric radiative heating is largely

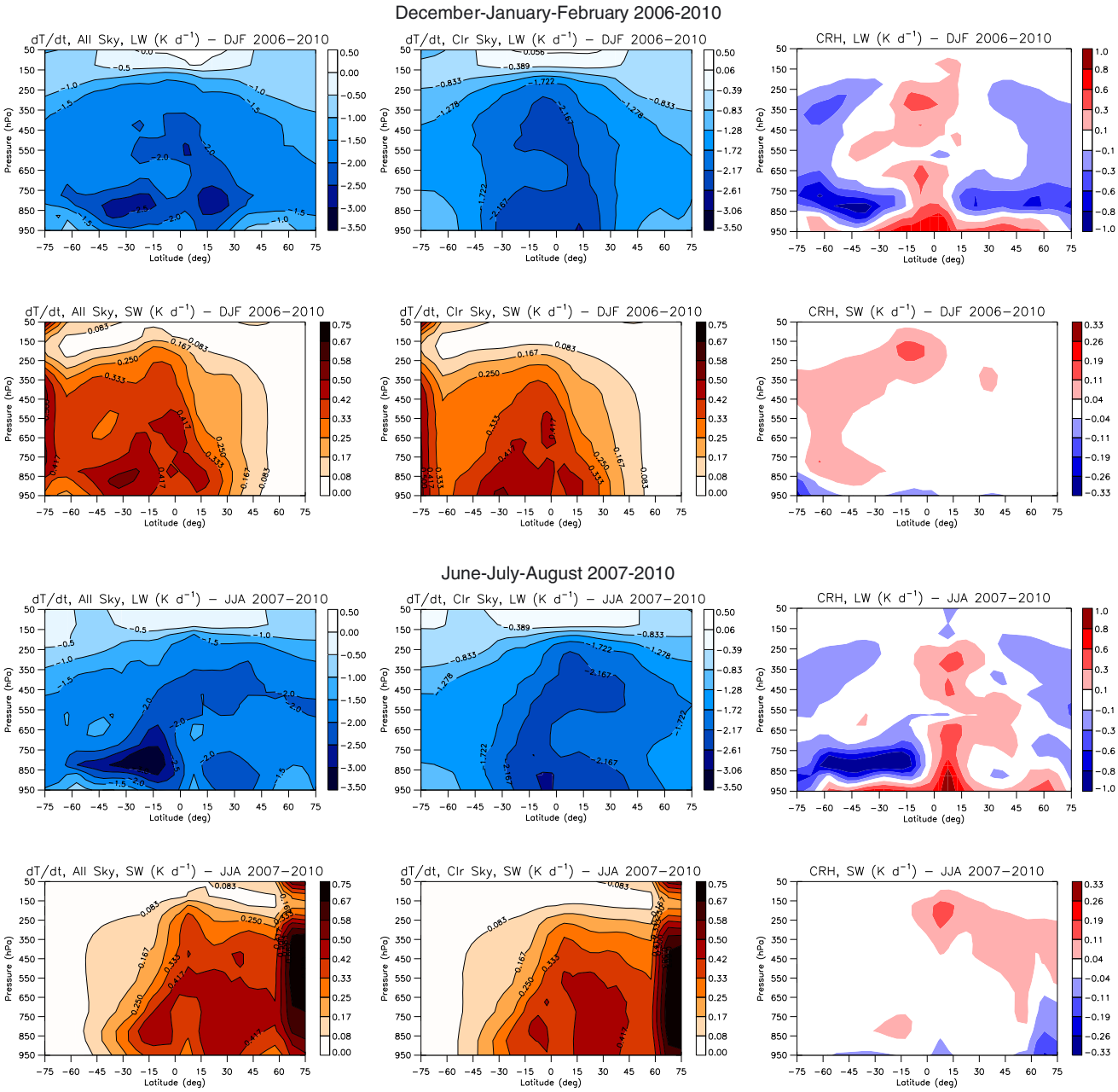

Figure 3. For DJF 2006–2010: All-sky LW, clear-sky LW, and LW cloud radiative heating (CRH) (first row); as previous for SW (second row). The third and fourth rows are as above, but for JJA 2007–2010. Note that the LW and SW CRH plots use different scales.

a reflection of the Earth's mean water vapor distribution, with sharp vertical gradients introduced by clouds. These sharp gradients are largely absent in passive-sensor derived flux/heating data sets such as those based on CERES.

[23] Analysis of the total atmospheric radiative heating reveals a minimum in cooling in the tropical lower to middle troposphere, a cooling maximum in the upper-boundary layer of the Southern Hemisphere poleward of −10° latitude, and a minimum in cooling in the lower boundary layer in the middle to high latitudes of both hemispheres. The annual mean cloud radiative heating is driven largely by longwave absorption and emission by clouds. Clouds tend to radiatively heat the atmosphere in the lower boundary layer due to cloud base warming effects. In the tropics, this heating extends into the middle troposphere, turns to a cooling near the freezing level, and reverts to heating upward toward the tropopause. In the midlatitudes extending into polar regions, clouds tend to strongly cool the upper-boundary layer all year in the Southern Hemisphere and primarily during the winter in the Northern Hemisphere. This hemispheric asymmetry reflects the larger seasonal cycle in Northern Hemisphere cloudiness and greater corresponding clear-sky cooling (see, for example, *Masunaga and L'Ecuyer* [2010]). Clouds tend to cool the midlatitude and polar atmosphere above the boundary layer as well.

[24] In summary, these new observation-based estimates of radiative heating contrast with pre-CloudSat/CALIPSO observations in that they provide cloud radiative heating at

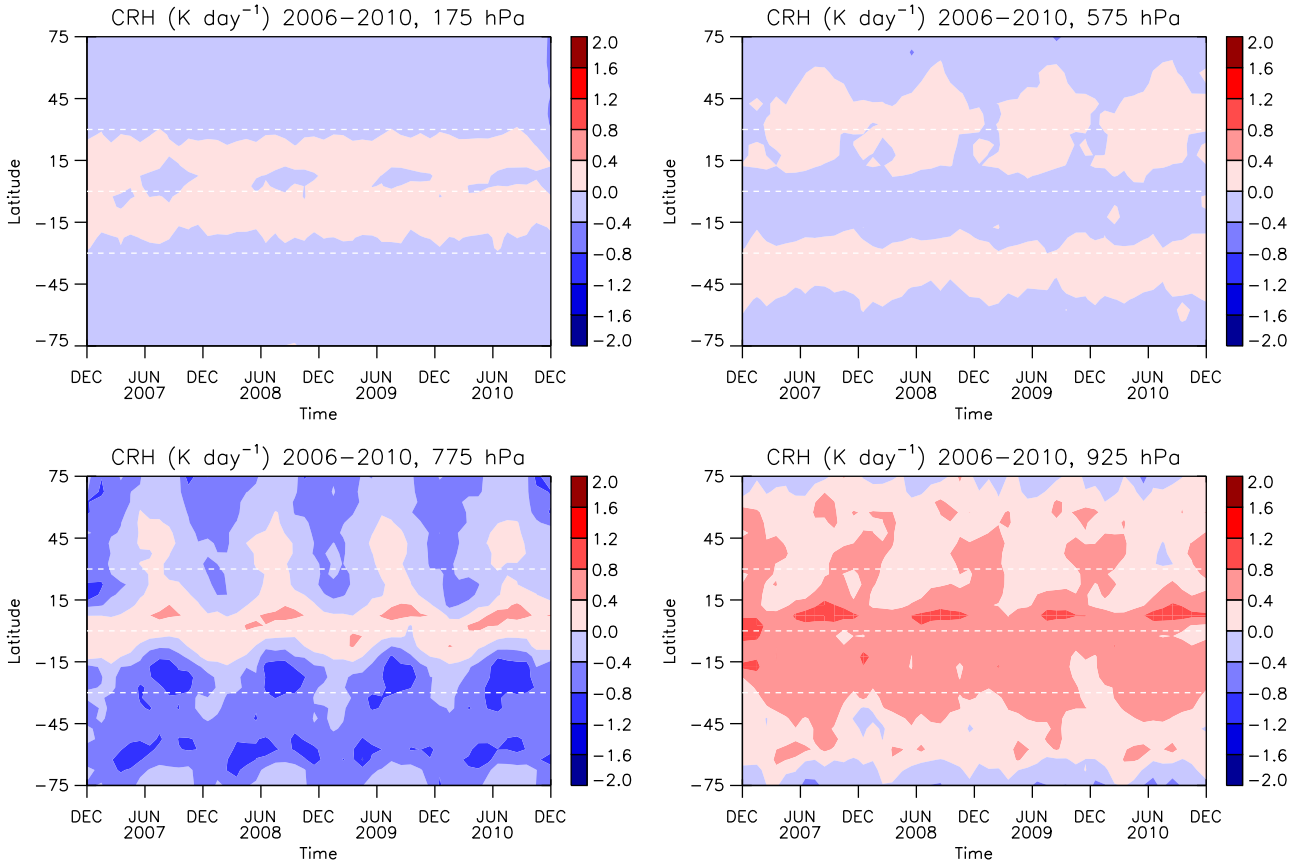

Figure 4. Hovmöller diagrams of cloud radiative heating (CRH) at four vertical levels for the 4 year period beginning December 2006.

a much higher vertical resolution than previous studies, revealing detailed heating structures (including hemispheric and seasonal asymmetries) that were previously not resolvable using passive remote sensing instruments. The large and persistent cloud-driven vertical heating gradients over the Southern Ocean, for example, are of special interest since climate models generally poorly replicate the observed radiation balance in this region [*Trenberth and Fasullo*, 2010]. These new observations can also contribute to our understanding of the planetary general circulation since diabatic heating is a key ingredient in the production of atmospheric potential energy that is eventually dissipated by cyclones [*Lorenz*, 1955].

[25] **Acknowledgments.** We thank the CloudSat and CALIPSO science teams for making measurements of this type possible. Data were provided by the CloudSat Data Processing Center at the Cooperative Institute for Research in the Atmosphere. This work was performed under NASA Grant NNX10AM19G.

References

Davis, P. A. (1963), An analysis of the atmospheric heat budget, *J. Atmos. Sci.*, *20*(1), 5–22.

Hartmann, D. L., and D. A. Short (1980), On the use of Earth radiation budget statistics for studies of clouds and climate, *J. Atmos. Sci.*, *37*(6), 1233–1250, doi:10.1175/1520-0469(1980)037<1233:OTUOER>2.0.CO;2.

Haynes, J. M., C. Jakob, W. B. Rossow, G. Tselioudis, and J. Brown (2011), Major characteristics of Southern Ocean cloud regimes and their effects on the energy budget, *J. Climate*, *24*(19), 5061–5080.

Haynes, J. M., and G. L. Stephens (2007), Tropical oceanic cloudiness and the incidence of precipitation: Early results from CloudSat, *Geophys. Res. Lett.*, *34*, L09811, doi:10.1029/2007GL029335.

Henderson, D., T. L'Ecuyer, G. Stephens, P. Partain, and M. Sekiguchi (2012), A multi-sensor perspective on the radiative impacts of clouds and aerosols, *J. Appl. Meteor. Climatol.*, doi:10.1175/JAMC-D-12-025.1, in press.

Johnson, R. H., T. M. Rickenbach, S. A. Rutledge, P. E. Ciesielski, and W. H. Schubert (1999), Trimodal characteristics of tropical convection, *J. Climate*, *12*, 2397–2418.

Johnson, R. H., and G. S. Young (1983), Heat and moisture budgets of tropical mesoscale anvil clouds, *J. Atmos. Sci.*, *40*, 2138–2147.

Kato, S., F. G. Rose, and T. P. Charlock (2005), Computation of domain-averaged irradiance using satellite-derived cloud properties, *J. Atmos. Oceanic Technol.*, *22*(2), 146–164.

Kuhn, P. M., and V. E. Suomi (1960), Infrared radiometer soundings on a synoptic scale, *J. Geophys. Res.*, *65*(11), 3669–3677.

L'Ecuyer, T. S., N. B. Wood, T. Haladay, G. L. Stephens, and P. W. Stackhouse (2008), Impact of clouds on atmospheric heating based on the R04 CloudSat fluxes and heating rates data set, *J. Geophys. Res.*, *113*(D8), D00A15, doi:10.1029/2008JD009951.

Lorenz, E. N. (1955), Available potential energy and the maintenance of the general circulation, *Tellus*, *7*(2), 157–167.

Mace, G. G. (2010), Cloud properties and radiative forcing over the maritime storm tracks of the Southern Ocean and North Atlantic derived from A-Train, *J. Geophys. Res.*, D10201, doi:10.1029/2009JD012517.

Mace, G. G., Q. Q. Zhang, M. Vaughan, R. Marchand, G. Stephens, C. Trepte, and D. Winker (2009), A description of hydrometeor layer occurrence statistics derived from the first year of merged Cloudsat and CALIPSO data, *J. Geophys. Res.*, *114*, D00A26, doi:10.1029/2007JD009755.

Manabe, S., and R. F. Strickler (1964), Thermal equilibrium of the atmosphere with a convective adjustment, *J. Atmos. Sci.*, *21*(4), 361–385.

Masunaga, H., and T. S. L'Ecuyer (2010), Equatorial asymmetry of the East Pacific ITCZ: Observational constraints on the underlying processes, *J. Climate*, *24*(6), 1784–1800.

McFarlane, S. A., J. H. Mather, and T. P. Ackerman (2007), Analysis of tropical radiative heating profiles: A comparison of models and observations, *J. Geophys. Res.*, *112*(D14), D14218, doi:10.1029/2006JD008290.

Rossow, W. B., and Y. C. Zhang (1995), Calculation of surface and top of atmosphere radiative fluxes from physical quantities based on ISCCP data sets 2. Validation and first results, *J. Geophys. Res.*, *100*, 1167–1197.

Sabatini, R. R., and V. E. Suomi (1962), On the possibility of atmospheric infrared cooling estimates from satellite observations, *J. Atmos. Sci.*, *19*(4), 349–350.

Slingo, A., and J. M. Slingo (1988), The response of a general circulation model to cloud longwave radiative forcing. I: Introduction and initial experiments, *Q. J. R. Meteorol. Soc.*, *114*(482), 1027–1062.

Slingo, J. M., and A. Slingo (1991), The response of a general circulation model to cloud longwave radiative forcing. II: Further studies, *Q. J. R. Meteorol. Soc.*, *117*(498), 333–364.

Stephens, G. L., et al. (2002), The cloudsat mission and the A-train—A new dimension of space-based observations of clouds and precipitation, *Bull. Am. Meteorol. Soc.*, *83*, 1771–1790.

Stephens, G. L., et al. (2008), CloudSat mission: Performance and early science after the first year of operation, *J. Geophys. Res.*, *113*, D00A18, doi:10.1029/2008JD009982.

Stephens, G. L., J. Li, M. Wild, C. A. Clayson, N. Loeb, S. Kato, T. L'Ecuyer, P. W. Stackhouse, M. Lebsock, and T. Andrews (2012), An update on Earth's energy balance in light of the latest global observations, *Nat. Geosci.*, *5*(10), 691–696.

Suomi, V. E., and P. M. Kuhn (1958), An economical net radiometer, *Tellus*, *10*(1), 160–163.

Tanelli, S., S. L. Durden, E. Im, K. S. Pak, D. G. Reinke, P. Partain, J. M. Haynes, and R. T. Marchand (2008), CloudSat's cloud profiling radar after two years in orbit: Performance, calibration, and processing, *IEEE Trans. Geosci. Remote Sens.*, *46*, 3560–3573.

Trenberth, K. E., and J. T. Fasullo (2010), Simulation of present-day and twenty-first-century energy budgets of the Southern Oceans, *J. Climate*, *23*, 440–454.

Vonder Haar, T. H., and V. E. Suomi (1971), Measurements of the Earth's radiation budget from satellites during a five-year period. Part I: Extended time and space means, *J. Atmos. Sci.*, *28*(3), 305–314.

Wielicki, B. A., B. R. Barkstrom, E. F. Harrison, R. B. Lee, G. Louis Smith, and J. E. Cooper (1996), Clouds and the Earth's Radiant Energy System (CERES): An earth observing system experiment, *Bull. Amer. Meteor. Soc.*, *77*(5), 853–868.

Winker, D. M., W. Hunt, and C. Hostetler (2007), Initial performance assessment of CALIOP, *Geophys. Res. Lett.*, *34*, L19803, doi:10.1029/2007GL030135.

Zhang, Y. C., W. B. Rossow, and A. A. Lacis (1995), Calculation of surface and top of atmosphere radiative fluxes from physical quantities based on ISCCP data sets. 1. Method and sensitivity to input data uncertainties, *J. Geophys. Res.*, *100*, 1149–1165.

Zhang, Y. C., W. B. Rossow, A. A. Lacis, V. Oinas, and M. I. Mishchenko (2004), Calculation of radiative fluxes from the surface to top of atmosphere based on ISCCP and other global data sets: Refinements of the radiative transfer model and the input data, *J. Geophys. Res.*, *109*, D19105, doi:10.1029/2003JD004457.